JGR Solid Earth

RESEARCH ARTICLE
10.1029/2021JB023170

Elasticity of Hydrated Al-Bearing Stishovite and Post-Stishovite: Implications for Understanding Regional Seismic V_S Anomalies Along Subducting Slabs in the Lower Mantle

Yanyao Zhang[1], Suyu Fu[1,2], Shun-ichiro Karato[3], Takuo Okuchi[4], Stella Chariton[5], Vitali B. Prakapenka[5], and Jung-Fu Lin[1]

[1]Department of Geological Sciences, Jackson School of Geosciences, The University of Texas at Austin, Austin, TX, USA, [2]School of Earth and Space Exploration, Arizona State University, Tempe, AZ, USA, [3]Department of Earth and Planetary Sciences, Yale University, New Haven, CT, USA, [4]Institute for Integrated Radiation and Nuclear Science, Kyoto University, Osaka, Japan, [5]Center for Advanced Radiation Sources, The University of Chicago, Chicago, IL, USA

Key Points:

- Elastic moduli across the Al,H-bearing post-stishovite transition are derived from high-pressure Raman and X-ray diffraction data
- Stishovite with 1.3 mol% Al and 0.6 mol% H undergoes the post-stishovite transition at ~1,060 km depth with −29% V_S anomaly
- V_S reductions across the Al,H-bearing post-stishovite transition can explain regional seismic V_S anomalies along some subducting slabs

Supporting Information:

Supporting Information may be found in the online version of this article.

Correspondence to:

J-F. Lin and Y. Zhang,
afu@jsg.utexas.edu;
yanyaozhang@utexas.edu

Citation:

Zhang, Y., Fu, S., Karato, S. -i., Okuchi, T., Chariton, S., Prakapenka, V. B., & Lin, J.-F. (2022). Elasticity of hydrated Al-bearing stishovite and post-stishovite: Implications for understanding regional seismic V_S anomalies along subducting slabs in the lower mantle. *Journal of Geophysical Research: Solid Earth*, *127*, e2021JB023170. https://doi.org/10.1029/2021JB023170

Received 3 SEP 2021
Accepted 3 APR 2022

Abstract Seismic studies have found seismic scatterers with −2 to −12% shear velocity anomalies along some subducting slabs at 700–1900 km depth. The ferroelastic post-stishovite transition in subducted mid-ocean ridge basalt (MORB) has been linked to these seismic features, but compressional and shear wave velocities (V_P and V_S) and full elastic moduli (C_{ij}) of Al,H-bearing stishovite and post-stishovite at high pressure remain uncertain. Here we have determined Raman shifts of optic modes and equation of state parameters of two hydrated Al-bearing stishovite crystals, Al1.3-SiO_2 (1.34 mol% Al and 0.55 mol% H) and Al2.1-SiO_2 (2.10 mol% Al and 0.59 mol% H), up to ~70 GPa in diamond anvil cells coupled with Raman spectroscopy and X-ray diffraction. The experimental data are modeled using a pseudoproper Landau theory to derive full C_{ij} and sound velocities across the post-stishovite transition at high pressure. The Al and H dissolution in stishovite significantly reduces the transition pressure to 21.1 GPa in Al1.3-SiO_2 and to 16.1 GPa in Al2.1-SiO_2, where the transition is manifested by approximately 29% V_S reduction. Considering that stishovite with approximately 1.3 mol% Al and 0.6 mol% H could account for 20 vol% in subducted MORB at the top-lower mantle, the Al,H-bearing post-stishovite transition with a Clapeyron slope of 65 K/GPa would occur at about 1060 km depth with −7(4)% V_S anomaly. The V_S anomalies across the Al,H-bearing post-stishovite transition can help explain the seismically-observed depth-dependent V_S anomalies along some subducting slabs in the top- to mid-lower-mantle depths including the Tonga subducting slab.

Plain Language Summary Seismologists have found that shear wave travels 2%–12% slower along some regions of subducting slabs at 700–1,900 km depths than the surrounding lower mantle. This observation cannot be explained by the presence of cold subducting oceanic crusts alone, but the transition from stishovite to post-stishovite could be a possible cause. Stishovite is a high-pressure dense silica polymorph that makes up about one fifth volume of subducting mid-ocean ridge basalt in the lower mantle. We designed high-pressure Raman spectroscopy and X-ray diffraction experiments to probe lattice vibration modes and lattice parameters, respectively, of Al,H-bearing stishovite and post-stishovite. These results are used to evaluate the speed of sound across the post-stishovite transition. Our study shows that the shear wave velocity of stishovite with 1.3–2.1 mol% Al and 0.5–0.6 mol% H significantly slows down by −29% at 16–21 GPa. If one fifth volume of the subducting oceanic crust is made of stishovite with 1.3 mol% Al and 0.6 mol% H, the velocity reduction across the transition could be ~7% at ~1,060 km depth. Regional seismic observations of V_S anomalies along some subducting slabs in the top- to mid-lower mantle can be explained by the presence of the Al,H-bearing post-stishovite transition.

1. Introduction

Seismic tomographic studies have revealed wide-spread stagnant slabs in the mantle beneath subduction zones (Fukao & Obayashi, 2013). The subducting slabs contain Mid-Ocean Ridge Basalt (MORB) and other crustal and sedimentary materials that are chemically and physically distinct from the lithospheric mantle (Ringwood, 1975). As slab subduction occurs deeper into the lower mantle, basaltic materials are expected to exhibit distinct mineralogy and physical properties that may be revealed seismically (Ishii et al., 2019; Rost et al., 2008). Compared with the mantle lithosphere of approximately 100–200 km thick, the oceanic crust is only ~7 km thick

so interpretations of seismic images for the subducting MORB materials in the lower mantle have been challenging. Specifically, global seismic tomography has a length resolution of hundreds of kilometers that could not be used to detect the subducted basalt (or eclogite) in the mantle (Fukao & Obayashi, 2013). On the other hand, analyses of short period seismic-wave scattering can provide a much better spatial resolution in the order of ~10 km in the mantle (Rost et al., 2008). Insofar, these short period seismic studies have revealed the occurrence of many regional seismic scatterers with a number of distinct features: (a) slower shear wave velocity (V_S) anomaly up to ~12% reduction, no significant compressional wave velocity (V_P) anomaly, and sometimes higher density (ρ) anomaly at 700–1,900 km depth (Niu, 2014; Niu et al., 2003); (b) planar geometry with several to tens of kilometers in thickness and tens to hundreds of kilometers in length; (c) occurrence within or beneath the subduction slab along the circum-Pacific region, but the frequency of observations decreases from top- to mid-lower mantle (Haugland et al., 2017; Kaneshima, 2019; Li & Yuen, 2014; Vinnik et al., 2001). These features are thought to be indicative of the presence of ancient subducted basalts in the lower mantle (Kaneshima & Helffrich, 1999).

To decipher the aforementioned seismic observations at depths, sound velocities and densities of major constituent minerals at relevant pressure-temperature (*P-T*) conditions of the subducted slabs are critically needed. Subducted MORB materials at the upper part of the lower mantle are expected to contain approximately 20 vol% stishovite, 30 vol% $CaFe_2O_4$-type phase (CF) or new hexagonal phase (NAL), 30 vol% bridgmanite (Bgm), and 20 vol% Ca-perovskite (CaPv; Ishii et al., 2019). Previous studies have shown that sound velocities of these phases except stishovite fall between those of bridgmanite and ferropericlase, the two most abundant minerals in a pyrolite compositional model in the lower mantle (Gréaux et al., 2019; Wu et al., 2016; Xu et al., 2008; Yang et al., 2015). That is, their velocity characteristics could not be used to reconcile the observations of small-scale seismic V_S anomalies along subducting slabs in the lower mantle. However, their occurrence could contribute to seismic observations of enhanced densities in some regions (Hirose et al., 2005; Niu, 2014; Niu et al., 2003; Sun et al., 2016). On the other hand, the rutile-type stishovite displays much higher sound velocities than typical mantle minerals (Yang & Wu, 2014; Zhang et al., 2021), although its density is similar to that of mineral aggregates in a pyrolite composition (Fischer et al., 2018; Irifune et al., 2010). Stishovite undergoes a pseudoproper ferroelastic transition to a $CaCl_2$-type post-stishovite phase with a spontaneous strain (Carpenter et al., 2000; Hemley et al., 2000). For pure-endmember stishovite (SiO_2), the distortion transition occurs at 55 GPa and 300 K and is associated with a drastic V_S reduction of −26% and a mild V_P reduction of −10%, but the density continuously increases with increasing pressure (Zhang et al., 2021). It has been theoretically shown that subducted MORB with 20 vol% stishovite undergoing the post-stishovite transition could produce a V_S reduction of up to ~6.5% and a V_P reduction of up to ~1.5% at the mid-lower-mantle depth that can help explain seismic wave velocities (Wang et al., 2020). However, the post-stishovite transition has a positive Clapeyron slope of 65 K/GPa and would occur at ~1,800 km depth at relevant *P-T* conditions of a cold subducting slab (77 GPa and 1706 K; Fischer et al., 2018). The transition depth is thus too deep to be consistent with these aforementioned regional seismic V_S anomalies at shallower lower mantle depths.

Based on previous geochemical and petrological studies (Gale et al., 2013), subducted MORB materials can contain ~10–19 wt% alumina (or ~4.3–8.1 mol%) which can partition into stishovite crystals. Multi-anvil apparatus experiments on element partitioning in a basaltic system have revealed that the Al content in stishovite increases from ~0.5 mol% at 22 GPa to ~1.5 mol% at 33 GPa (Ishii et al., 2019; Ono et al., 2001). Additionally, chemical analysis of mineral inclusions in natural diamonds from the subducted ecologitic assemblage also shows the presence of nearly Al-free silica (≤0.06 mol% Al) in association with Al_2SiO_5 phase (Zedgenizov et al., 2015). This indicates the possible presence of Al-bearing stishovite at lower-mantle depths, although naturally occurring Al-bearing stishovite has not been reported. In addition to the Al substitution, subducting slabs can contain a small amount of water in hydrous or nominally anhydrous minerals (NAMs) in the mantle. In multi-anvil apparatus experiments, Fourier-transform infrared spectroscopy (FTIR) analyses showed that Al-bearing stishovite crystals contain approximately 0.03–0.67 mol% H at 20–26 GPa and 1,473–2,073 K conditions (Litasov et al., 2007).

The Al^{3+} and/or H^+ incorporation in stishovite can reduce the post-stishovite transition pressure to the depth range more consistent with the seismic observations of the regional V_S anomalies in the shallow lower mantle (Lakshtanov et al., 2007b; Umemoto et al., 2016). Although full elasticity of pure stishovite and post-stishovite and the effect of Al on the post-stishovite transition pressure have been relatively well investigated (Asahara et al., 2013; Karki et al., 1997; Lakshtanov et al., 2007b; Li et al., 1996; Shieh et al., 2002; Yang & Wu, 2014; Zhang et al., 2021), elasticity data of hydrated Al-bearing stishovite across the post-stishovite transition remain

largely unexplored (Bolfan-Casanova et al., 2009; Gréaux et al., 2016; Lakshtanov et al., 2007a). This is mainly due to the technical difficulty in measuring sound velocities and reliably deriving full elastic moduli (C_{ij}) of the stishovite crystal at high pressure (Zhang et al., 2021). Alternatively, high-pressure experimental results on Raman shifts of optic modes and equations of state (EOS) parameters across the post-stishovite transition can be used to evaluate full C_{ij} using Landau theory modeling (Carpenter et al., 2000). The full C_{ij} data can then be used to calculate sound velocities and other elastic parameters across the post-stishovite transition as a function of pressure.

In this study, we have measured Raman shifts of major optic modes and lattice parameters of two hydrated Al-bearing stishovite single crystals, Al1.3-SiO_2 (1.34 mol% Al and 0.55 mol% H) and Al2.1-SiO_2 (2.10 mol% Al and 0.59 mol% H), up to ~70 GPa in high-pressure diamond anvil cells. The experimental data are modeled with a pseudoproper Landau theory in which some Landau parameters have been well constrained using a recent experimental elasticity study of stishovite at high pressure (Zhang et al., 2021). These combined experimental and modeling approaches allow us to determine full elastic properties of the Al,H-bearing stishovite, including C_{ij}, adiabatic bulk and shear moduli (K_S and μ), aggregate sound velocities (V_S and V_P), and Poisson's ratio (ν), across the post-stishovite transition at high pressure. Our results show that the post-stishovite transition occurs at 21.1 GPa in Al1.3-SiO_2 and 16.1 GPa in Al2.1-SiO_2, where the B_{1g} optic mode softens and the elastic moduli C_{11} and C_{12} merge together. The full C_{ij} and sound velocities of hydrated Al-bearing stishovite and post-stishovite from high-pressure Raman and X-ray diffraction measurements are used to provide new constraints on Al/H-dependent post-stishovite transition and associated velocity changes at high *P-T*. Assuming that subducted MORB materials contain 20 vol% stishovite with 1.3 mol% Al and 0.6 mol% H, our results show that the post-stishovite transition can exhibit a V_S reduction of −7(4)%. We have further modeled the V_S anomaly of the post-stishovite transition as a function of Al contents at high *P-T*. These results are compared with regional seismic observations in some selected subduction zone settings including the Tonga slab. Our results provide new insights into the regional seismic V_S anomalies that can be explained by the hydrated Al-bearing post-stishovite transition from the top- to mid-lower mantle.

2. Experimental Details

Al,H-bearing stishovite crystals were synthesized at the Institute for Planetary Materials at Okayama University. Two starting samples were prepared by mixing silica powder of 99.99% purity with 10 wt% gibbsite $Al(OH)_3$ in run# 5K3302 and with 13 wt% gibbsite $Al(OH)_3$ in run# 1K2965. Each starting mixture was loaded into a platinum capsule of 4 mm in length and 2 mm in outer diameter. The sample assemblage in run# 5K3302 with a $LaCrO_3$ heater was compressed to 20 GPa and then heated to 1973 K for 16.5 hr in a 5000-ton Kawai-type multi-anvil apparatus. The assemblage in run# 1K2965 with the same type of heater was compressed to 19.2 GPa and heated to 1973 K for 7 hr using a 1,000-ton Kawai-type multi-anvil apparatus. Detailed information about the sample assemblage and apparatus conditions can be found in the literature (Okuchi et al., 2015; Xu et al., 2017). Stishovite crystals extracted from the Pt capsules are anhedral to subhedral in shape and are about tens to hundreds of micrometers in length under an optical microscope. A few crystals of approximately 100–200 μm in diameters were selected for compositional analysis using a JEOL Electron Microprobe (EPMA) and a Scanning Electron Microscopy with Energy Dispersive X-Ray Spectroscopy (SEM/EDS) in the Department of Geological Sciences at the University of Texas at Austin (UT Austin). Chemical mappings on Si, Al, and O elements show compositional homogeneities throughout the crystals (Figure S1 in Supporting Information S1). Quantitative results from Wavelength-Dispersive Spectroscopy (WDS) analysis show Al contents of 1.34(2) mol% (or 3.43(6) wt% Al_2O_3 averaged from 5 analyses) in the Al1.3-SiO_2 crystal from run# 5K3302 and 2.10(2) mol% (or 5.37(4) wt% Al_2O_3 averaged from 8 analyses) in Al2.1-SiO_2 from run# 1K2965 (Table S1 in Supporting Information S1). Other elements are below the detection limit of the analytical techniques used here.

Synchrotron X-ray diffraction (XRD) measurements are used to determine structures and lattice parameters of the crystals at the beamline 13ID-D of the GSECARS, Advanced Photon Source (APS), Argonne National Laboratory. A few Al1.3-SiO_2 and Al2.1-SiO_2 crystals were polished down to approximately 10–15 μm thick platelets, and then loaded into a sample chamber in a diamond anvil cell with a pair of 300 μm flat culets. The sample chamber was made of a rhenium gasket with an initial thickness of 260 μm that was pre-indented to ~32 μm thickness and subsequently a hole of 190 μm diameter was drilled in it. Au powder (Goodfellow; 99.95% purity)

of ~8 × 10 μm^2 grain size was also loaded next to the crystals in the sample chamber and used as the pressure calibrant (Fei et al., 2007). Neon pressure medium was loaded into the sample chamber using the gas loading system in the Mineral Physics Laboratory, UT Austin. The neon medium provides a quasi-hydrostatic environment in the sample chamber within our investigated pressure range (Kingma et al., 1995). An incident X-ray beam with a wavelength of 0.3344 Å was focused down to a beam size of ~3 × 3 μm^2 (FWHM) at the sample position where the diffracted signals were collected by a CdTe Pilatus 1M detector. During the data collection, the sample stage was rotated ±15° about its vertical axis to cover as many reflection spots as possible. The collected images were further integrated into one-dimensional spectra using the DIOPTAS software (Prescher & Prakapenka, 2015). Pressure uncertainties were evaluated from the EOS of Au in the experiments.

High-pressure Raman measurements were performed using a Renishaw InVia Raman spectroscopy system at the Mineral Physics Laboratory, UT Austin. A pair of anvils with 300 μm flat culets and ultralow fluorescence background were selected for the experiments. Similar to the sample preparation in aforementioned XRD experiments, Al1.3-SiO_2 and Al2.1-SiO_2 platelets of 10–15 μm thick and ~20 × 40 μm^2 grain size were loaded into a sample chamber with Ne pressure medium. A few ruby spheres were also loaded in the chamber and used as the pressure calibrant (Fei et al., 2007). The Raman system is equipped with a green excitation laser of 532 nm wavelength, a grating of 2400-line/mm, and a spectral resolution of 1.2 cm^{-1}. The system was calibrated using the Raman peak of a reference Si crystal at 520 cm^{-1} before high-pressure measurements. Each Raman spectrum was collected using a 20X objective with a focused beam width of ~2–3 μm, an exposure time of 15 s, and 20–30 accumulations. Pressure uncertainties of the experiments were evaluated from multiple ruby fluorescence measurements before and after each set of the Raman collection. Water contents in the crystals were also evaluated using unpolarized FTIR spectra taken in a Thermo Electron 6700 FTIR spectrometer with a connected FTIR Continuum microscope in the Department of Earth Sciences at the National Cheng Kung University. Raman spectra of the OH-stretching band regions of the Al,H-bearing stishovite crystals were also measured at ambient conditions.

3. Results

3.1. Al and H Substitution in the Rutile-Type Stishovite

Combined results of FTIR, Raman, electron microprobe and XRD spectral measurements are useful to examine Al and H substitutions in hydrated Al-bearing stishovite crystal structure (Figure 1). Analysis of XRD spectra of the synthesized crystals reveals the tetragonal rutile-type crystal structure with $P4_2/mnm$ space group at ambient conditions. Refined lattice parameters of the Al1.3-SiO_2 crystal are a = 4.1963(8) Å, c = 2.6723(4) Å, and V = 47.06(2) Å^3 while the Al2.1-SiO_2 crystal displays a = 4.2025(9) Å, c = 2.6788(16) Å, and V = 47.31(2) Å^3. Our results are consistent with the literature data in which the unit-cell volume of stishovite linearly expands with increasing Al content (Figure 1c; Lakshtanov et al., 2007b; Litasov et al., 2007). The lattice expansion can be mainly related to the coupled $2Al^{3+}$ and O_V^{2+} (oxygen vacancy) substitution for $2Si^{4+}$ in stishovite (Lakshtanov et al., 2007a). On the other hand, analysis of unpolarized FTIR and Raman spectra shows three major OH-stretching bands at ~2660, ~3140, and ~3410 cm^{-1}, consistent with literature data (Figures 1a and 1b; Litasov et al., 2007). The strongest FTIR absorption band at 3,140 cm^{-1} is also extremely intense in Raman measurements, revealing itself as an active FTIR and Raman mode. This is also the case for the modes at 2,660 and 3,410 cm^{-1}. The occurrence of the bands has been explained to be indicative of the coupled $Al^{3+} + H^+$ and/or pure $4H^+$ substitution for Si^{4+} in the structure, which are also expected to contribute to the expansion of the lattice (Nisr et al., 2017; Spektor et al., 2011). The water content C_{OH} of the crystals in the unpolarized spectra can be determined using a calibration method by Paterson (1982):

$$C_{OH} = \frac{X_i}{150\gamma} \int \frac{k(\tilde{\nu})}{(3780 - \tilde{\nu})} d\nu \quad (1)$$

where X_i is the density factor, $X_i = 9/\rho \times 10^6$, with the density as 4,237 g/l and 4,211 g/l for Al1.3-SiO_2 and Al2.1-SiO_2, respectively; γ is the orientation factor which is set as 1/3 for the unpolarized measurements; $k(\tilde{\nu})$ is an absorption in cm^{-1} at each wavenumber $\tilde{\nu}$ in cm^{-1}. After subtracting the background and normalizing the sample thickness to 1 cm, the water contents in Al1.3-SiO_2 and Al2.1-SiO_2 crystals are determined as 0.55(11) mol% H (or 0.25(5) wt% H_2O) and 0.59(11) mol% H (or 0.27(5) wt% H_2O), respectively. Together with chemical

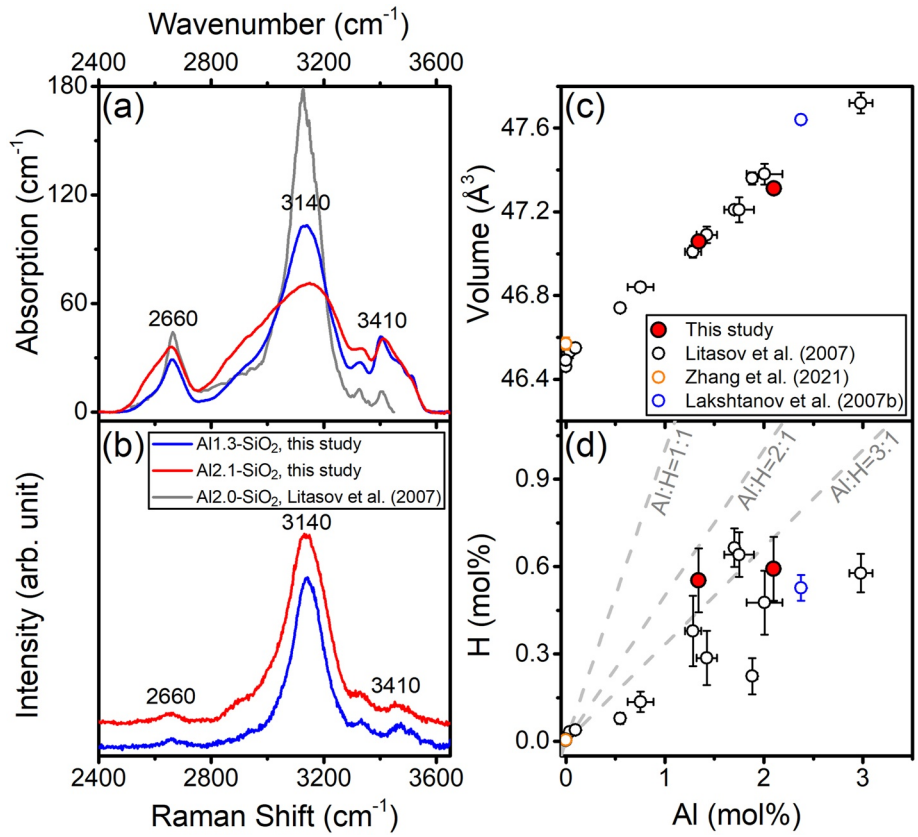

Figure 1. Characterizations of hydrated Al-bearing stishovite crystals. (a) and (b) show OH-stretching bands in Al1.3-SiO_2 (blue) and Al2.1-SiO_2 (red). (a) Representative unpolarized FTIR spectra; (b) representative Raman spectra. Wavenumbers and Raman shifts of OH-stretching bands were fitted and labeled next to major peaks in (a) and (b), respectively. (c) Unit-cell volume of stishovite as a function of Al content in mol% at ambient conditions. (d) H content as a function of Al content in mol% in stishovite. Gray dashed lines show three different Al/H ratios. Literature data are plotted for comparison (Lakshtanov et al., 2007b; Litasov et al., 2007; Zhang et al., 2021).

analysis results, the molar ratios of Al/H in these crystals are thus 2.4(7):1 and 3.5(8):1. These numbers are close to 2:1 and 3:1 ratio, but much larger than 1:1 ratio for the coupled $Al^{3+} + H^+$ substitution mechanism proposed previously (Pawley et al., 1993) (Figure 1d). These indicate that $2Al^{3+} + O_V^{2+} \leftrightarrow 2Si^{4+}$ mechanism is predominant in our Al,H-bearing stishovite crystals to expand the lattice, while the $Al^{3+} + H^+ \leftrightarrow Si^{4+}$ mechanism can help facilitate water incorporation into stishovite.

3.2. High-Pressure Raman Shifts of Major Optic Modes Across the Post-Stishovite Transition

Analyses of the Raman spectra of the crystals at ambient conditions show four intense optic Raman bands at 226, 583, 748, and 960 cm^{-1} in Al1.3-SiO_2 and at 224, 579, 744, and 957 cm^{-1} in Al2.1-SiO_2. After taking the Al substitution effects into account, these peaks can be assigned to B_{1g}, E_g, A_{1g}, and B_{2g} modes of the rutile-type stishovite, respectively (Kingma et al., 1995). The B_{1g}, E_g, and A_{1g} peaks can be well detected at high pressure, but the B_{2g} mode was blocked by the background of the diamond anvil (Tables S2–S4 in Supporting Information S1). Raman shifts of E_g and A_{1g} modes increase with increasing pressure whereas the Raman shifts of the B_{1g} mode decrease with increasing pressure (Figure 2). The trends and slopes of these Raman shifts are consistent with those in pure SiO_2 stishovite at high pressure (Kingma et al., 1995; Zhang et al., 2021). Crossing into the $CaCl_2$-type post-stishovite phase, the B_{1g} and A_{1g} evolve into two A_g modes but splitting of E_g mode into B_{2g} and B_{3g} modes was not observed due to background of the diamond anvil. Raman shifts of the A_g modes in the post-stishovite phase increase with increasing pressure, but the slope is shallower than that in pure SiO_2 stishovite (Figure 2c). Most importantly, the pressure-dependence of the stishovite's B_{1g} mode becomes positive in the

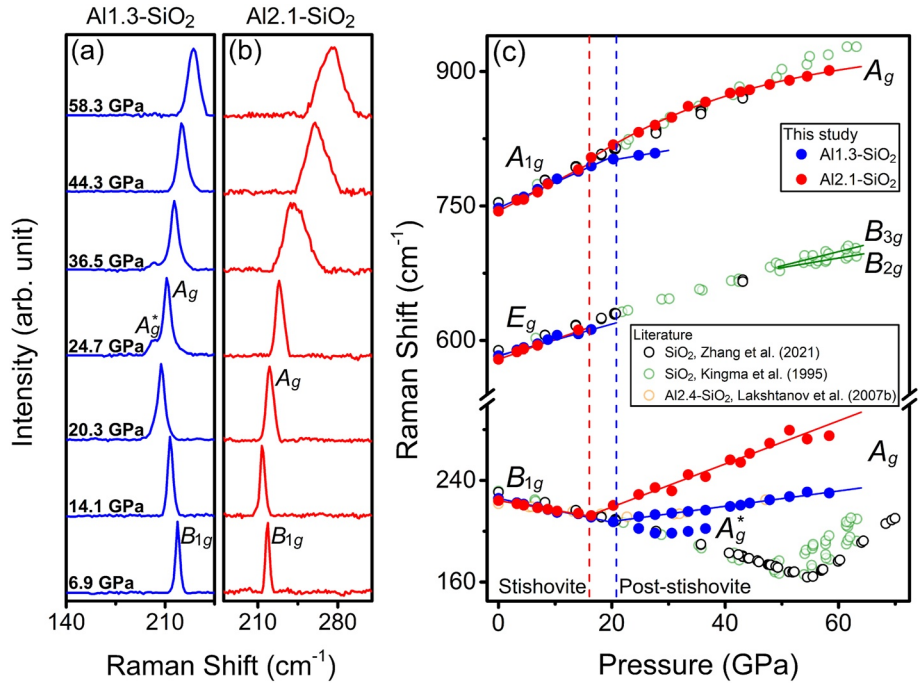

Figure 2. Raman shifts of Al,H-bearing stishovite and post-stishovite phases at high pressure. (a) and (b) are representative high-pressure Raman spectra of Al1.3-SiO_2 and Al2.1-SiO_2, respectively, with the B_{1g} optic mode in stishovite and the A_g and A_g* modes in post-stishovite. (c) Pressure-dependent Raman shifts for Raman modes of stishovite (B_{1g}, E_g, A_{1g}) and post-stishovite (A_g, A_g*, B_{2g}, B_{3g}). Solid lines are best linear or quadratic fits to our experimental data to guide the eye. Error bars are smaller than the symbols and are not shown for figure clarity. Previous studies on stishovite crystals with pure SiO_2 (Al free) and Al2.4-SiO_2 (2.4 mol% Al) compositions are plotted as open circles for comparison (Kingma et al., 1995; Lakshtanov et al., 2007b; Zhang et al., 2021). Vertical dashed lines show the transition pressure for each composition with the same color as the corresponding data in (a) or (b).

post-stishovite's A_g mode after the post-stishovite transition. A satellite band, denoted as A_g*, in the Al1.3-SiO_2 crystal occurs between 21.1 and 36.5 GPa (Figures 2a and 2c) with Raman shift behavior similar to the A_g mode, but the kink occurs at approximately 28 GPa. The occurrence of the satellite peak may be due to local clusters of Al-poor regions where the local domains can resist the ferroelastic transition to a higher pressure. This phenomenon across the ferroelastic transition has been reported in other binary systems (Salje, 1990).

3.3. Lattice Parameters Across the Post-Stishovite Transition

Analysis of the high-pressure XRD spectra from Al1.3-SiO_2 and Al2.1-SiO_2 crystals shows 10–15 reflections in the tetragonal stishovite phase with 2θ ranging from 6° to 24° (Figures 3a and 3b; Tables S5 and S6 in Supporting Information S1). The analyzed lattice parameters indicate that lengths of a and c axis and unit-cell volume (V) decrease with increasing pressure with slopes consistent with those in pure-endmember stishovite (Figures 3c and 3d). With increasing pressure, some representative diffraction peaks in the tetragonal structure split into the orthorhombic post-stishovite structure with *Pnnm* space group at 21.1 GPa for Al1.3-SiO_2 and 16.1 GPa for Al2.1-SiO_2. Specifically, tetragonal 211 and 311 reflections in Miller indices split into pairs of orthorhombic (211 and 121) and (311 and 131) reflections, respectively, in Al1.3-SiO_2 crystal (Figure 3a). Similarly, splitting of tetragonal 210, 211, 310, 311, 320, 410, 411, and 420 reflections was observed in Al2.1-SiO_2 crystal (Figure 3b). These mean that the a-axis of the tetragonal stishovite splits into a- and b-axis of orthorhombic post-stishovite at high pressure. Axial and bulk incompressibilities of the stishovite and post-stishovite phases at high pressure were further evaluated using the Birch-Murnaghan EOS (Birch, 1947; Table S7 in Supporting Information S1). Isothermal bulk modulus (K_{T0}) of Al1.3-SiO_2 and Al2.1-SiO_2 crystals at ambient conditions is lower than that in pure SiO_2 stishovite, but higher than that in pure SiO_2 post-stishovite. These indicate that the Al and H substitution softens the tetragonal structure in stishovite but stiffens the orthorhombic structure in post-stishovite.

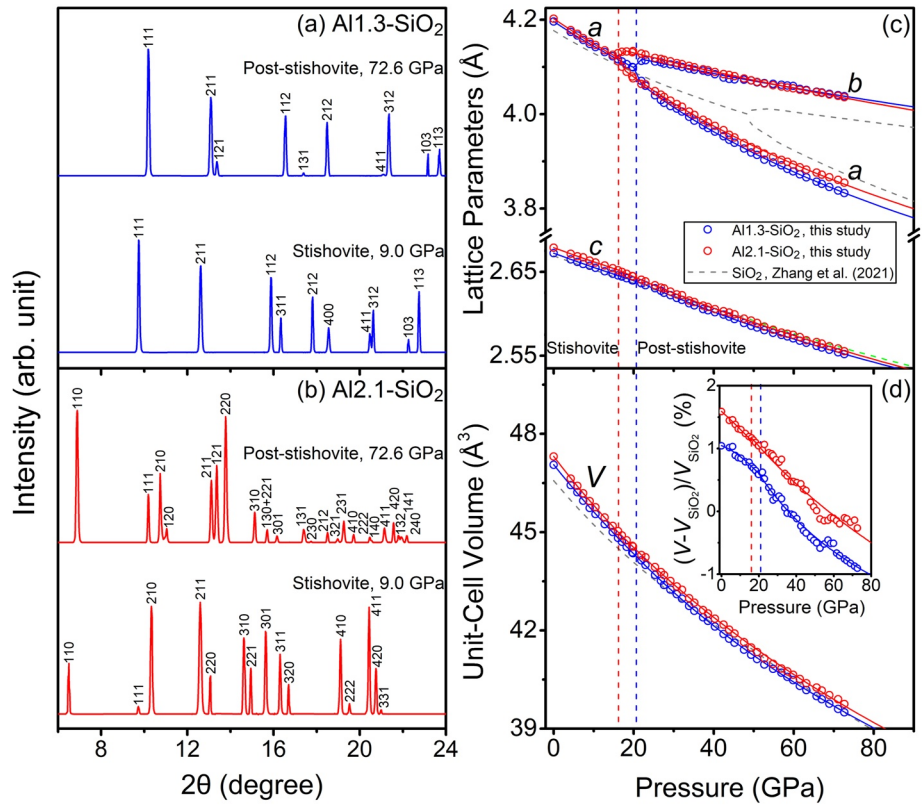

Figure 3. X-ray diffraction and equation of state results of hydrated Al-bearing stishovite and post-stishovite at high pressure. (a) and (b) are representative XRD patterns for Al1.3-SiO_2 and Al2.1-SiO_2 crystals, respectively, at 9.0 GPa for the stishovite phase and at 72.6 GPa for the post-stishovite phase. Miller indices hkl labeled next to identified diffraction peaks are used to calculate lattice parameters and unit-cell volumes, shown in (c) and (d). The occurrence of the post-stishovite phase is most visible in the splitting of some reflection peaks in the stishovite phase across the transition, such as a splitting of the 211 reflection into a pair of 211 and 121 reflections. (c) and (d) show lattice parameters and unit-cell volumes, respectively, of the stishovite and post-stishovite phases in Al1.3-SiO_2 (blue open circles) and Al2.1-SiO_2 (red open circles) at high pressure. Corresponding solid lines show best fits using the axial incompressibility or the Birch-Murnaghan equation of state (Birch, 1947). The insert panel shows unit-cell volume variations of the Al,H-bearing crystals at high pressure with respect to the endmember SiO_2 by Zhang et al. (2021). Vertical dashed lines show the transition pressures.

4. Discussion

4.1. Landau Theory Modeling of the Elasticity Across the Post-Stishovite Transition

Our high-pressure Raman and XRD results are used to derive full C_{ij} and sound velocities of the stishovite and post-stishovite phases. We use a pseudoproper-type Landau free energy expansion, where the order parameter Q is related to the soft B_{1g} optic mode and is coupled bilinearly with the symmetry-breaking spontaneous strain (Carpenter et al., 2000). In the modeling, a number of Landau parameters need to be well evaluated in order to reliably derive the full elastic moduli. These parameters include P_C^*, critical pressure (P_C), bare elastic moduli (C_{ij0}^0), pressure derivatives of C_{ij0}^0 ($C_{ij}^{0\prime}$), coupling coefficients (λ_i), and normal Landau coefficients (a and b). To start with, the intersection of the two linear fits to the squared Raman shifts of the B_{1g} and A_g modes as a function of pressure gives the P_C^* value at 21.1(6) GPa for Al1.3-SiO_2 and at 16.1(4) GPa for Al2.1-SiO_2 (Figure 4a). Extrapolation of the B_{1g} linear fit to zero Raman shift yields the P_C value where the optic mode becomes imaginary. Additionally, the C_{ij0}^0 can be calculated from literature C_{ij0} data of stishovite at ambient conditions after taking into account of the linear Al effect on the C_{ij0} in stishovite (Lakshtanov et al., 2007a). Since the pressure-dependent slopes for Raman shifts and lattice parameters are very similar in Al,H-bearing and pure SiO_2 stishovite (Figures 2c, 3c, and 3d), the C_{ij}^0 slope, the pressure derivatives of C_{ij}^0 ($C_{ij}^{0\prime}$), of the experimentally-determined values for pure SiO_2 endmember in a recent study can be used for the Al,H-bearing stishovite (Zhang et al., 2021). The exception here is for the $C_{11}^{0\prime}$ and $C_{12}^{0\prime}$ that can be affected by the shear softening and the transition

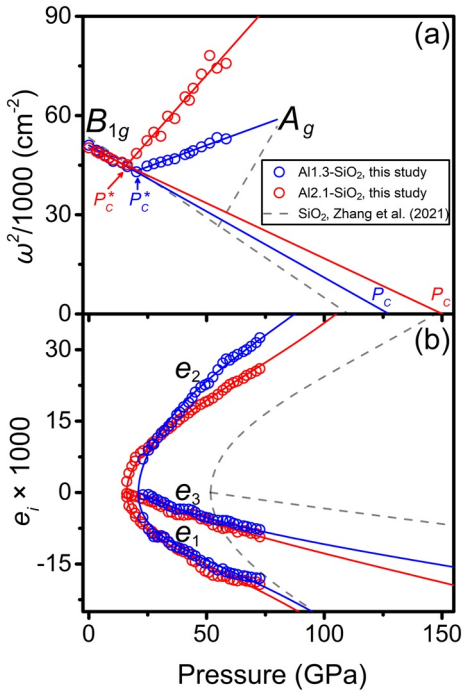

Figure 4. Landau theory modeling of the post-stishovite transition in hydrated Al-bearing stishovite. (a) Squared Raman shifts of B_{1g}→A_g modes divided by 1,000 (ω^2/1,000). The kink in the Raman shift slope reflects the post-stishovite transition pressure P_C* for each composition, while the linear extrapolation on ω^2/1,000 of the B_{1g} mode to zero yields the critical pressure P_C. (b) Spontaneous strains multiplied by 1,000 ($e_i \times 1{,}000$; $i = 1, 2, 3$). Blue and red circles are experimental data on Al1.3-SiO$_2$ and Al2.1-SiO$_2$, respectively, while corresponding lines are best fits. Literature results on endmember SiO$_2$ are shown as gray dashed lines (Zhang et al., 2021).

pressure such that these two parameters for the Al,H-bearing stishovite need to be evaluated in the modeling. Moreover, the coupling coefficients λ_4 and λ_6 are also set to those in the pure SiO$_2$ endmember because they are related to the spontaneous strains e_4, e_5, and e_6 that remain zero in the post-stishovite phase regardless of the Al and H contents due to the nature of the ferroelastic transition (Carpenter et al., 2000). In short, six parameters (coupling coefficients λ_1 and λ_3, Landau coefficients a and b, $C_{11}^{0\prime}$ and $C_{12}^{0\prime}$) are evaluated in our modeling using the Al and H dependent spontaneous strains e_1, e_2, and e_3 at high pressures that can be calculated from the lattice parameters (Figure 4b):

$$e_1 = \frac{a_{Pst} - a_{St}}{a_{St}}, e_2 = \frac{b_{Pst} - a_{St}}{a_{St}}, e_3 = \frac{c_{Pst} - c_{St}}{c_{St}} \tag{2}$$

where a_{Pst}, b_{Pst}, and c_{Pst} are lattice parameters of post-stishovite (*Pst*) at high pressure; a_{St} and c_{St} are the extrapolated lattice parameters of stishovite (*St*) at the same pressure. With all these Landau parameters determined (Table 1), the full set of C_{ij} of the stishovite and post-stishovite phases at high pressure can be calculated using the following expressions (Carpenter et al., 2000):

$$C_{11} = C_{11}^0 - \left(4\lambda_1^2 Q^2 + \lambda_2^2 + 4\lambda_1\lambda_2 Q\right)\chi \tag{3}$$

$$C_{22} = C_{11}^0 - \left(4\lambda_1^2 Q^2 + \lambda_2^2 - 4\lambda_1\lambda_2 Q\right)\chi \tag{4}$$

$$C_{33} = C_{33}^0 - 4\lambda_3^2 Q^2 \chi \tag{5}$$

$$C_{12} = C_{12}^0 - \left(4\lambda_1^2 Q^2 - \lambda_2^2\right)\chi \tag{6}$$

$$C_{13} = C_{13}^0 - \left(4\lambda_1\lambda_3 Q^2 + 2\lambda_2\lambda_3 Q\right)\chi \tag{7}$$

$$C_{23} = C_{13}^0 - \left(4\lambda_1\lambda_3 Q^2 - 2\lambda_2\lambda_3 Q\right)\chi \tag{8}$$

$$C_{44} = C_{44}^0 + 2\lambda_4 Q \tag{9}$$

$$C_{55} = C_{44}^0 - 2\lambda_4 Q \tag{10}$$

$$C_{66} = C_{66}^0 + 2\lambda_6 Q^2 \tag{11}$$

where χ is the susceptibility and Q is the order parameter as

$$\chi = \begin{cases} 1/\left[a\left(P - P_C\right)\right], & if\ P \le P_C^* \\ 1/\left[2ab\left(P_C^* - P\right)/b^* + a\left(P_C^* - P_C\right)\right], & if\ P > P_C^* \end{cases} \tag{12}$$

$$Q = \begin{cases} 0, & if\ P \le P_C^* \\ \sqrt{a\left(P_C^* - P\right)/b^*}, & if\ P > P_C^* \end{cases} \tag{13}$$

with the renormalized Landau coefficient b^* as

$$b^* = b - 2\left[\frac{\lambda_3^2\left(C_{11}^0 + C_{12}^0\right) + 2\lambda_1^2 C_{33}^0 - 4\lambda_1\lambda_3 C_{13}^0}{C_{33}^0\left(C_{11}^0 + C_{12}^0\right) - 2{C_{13}^0}^2}\right] \tag{14}$$

Standard deviations of the C_{ij}'s can be estimated using the equation for the standard error propagation (refer to Text S1 in Supporting Information S1 for details).

Table 1
Landau Model Parameters for the Stishovite to Post-Stishovite Transition

Compositions	Al1.3-SiO_2, 0.7 mol% H^+	Al2.1-SiO_2, 0.8 mol% H^+	SiO_2, 0.004 mol% H^+
References	This study	This study	Zhang et al. (2021)
P_C^*, GPa	21.1(6)	16.1(4)	55.0(10)
$(P_C - P_C^*)$, GPa	105.7(38)	134.3(65)	55.2(10)
a	−0.0512(49)	−0.0467(45)	−0.0501(29)
b, GPa	10.5(12)	10.6(14)	11
λ_1, GPa	−4.9(3)	−5.5(2)	11.03(85)
λ_2, GPa	60.5	78.5	27.61
λ_3, GPa	12.6(13)	12.2(11)	16.79(92)
λ_4, GPa	18.94	18.94	18.94(31)
λ_6, GPa	15.15	15.15	15.15(22)
C^0_{110}, GPa	999	1302	592.3
$C^{0\prime}_{11}$	10.0(9)	9.5(9)	10.80(47)
C^0_{120}, GPa	−375	−693	57.9
$C^{0\prime}_{12}$	9.9(7)	10.4(8)	8.81(63)
C^0_{130}, GPa	190.6	189.2	193.0
$C^{0\prime}_{13}$	2.91	2.91	2.91(27)
C^0_{330}, GPa	743.5	734.1	760.2
$C^{0\prime}_{33}$	7.07	7.07	7.07(48)
C^0_{440}, GPa	246.7	238.2	261.6
$C^{0\prime}_{44}$	3.18	3.18	3.18(5)
C^0_{660}, GPa	295.2	281.4	319.7
$C^{0\prime}_{66}$	5.60	5.60	5.60(13)

Note. See the main text for the meaning and references of Landau parameters listed in the first column. Numbers in parentheses represent ±1σ uncertainties.

We further calculate K_S and μ from our modeled C_{ij} values using Voigt–Reuss–Hill averaging scheme at high pressure (Hill, 1952). With ρ determined from EOS parameters (Table S7 in Supporting Information S1), the V_S and V_P values of stishovite and post-stishovite phases at each given pressure are calculated using the following equations:

$$V_P = \sqrt{\left(K_S + \frac{4}{3}\mu\right)/\rho},\ V_S = \sqrt{\mu/\rho} \tag{15}$$

The Poisson's ratio ν, a key seismic parameter reflecting the V_P and V_S ratio, is also calculated using the following equation:

$$\nu = \frac{1}{2}\left[\left(\frac{V_P}{V_S}\right)^2 - 2\right] \Big/ \left[\left(\frac{V_P}{V_S}\right)^2 - 1\right] \tag{16}$$

4.2. Al and H Effects on the Post-Stishovite Transition Boundary

The post-stishovite transition boundary influenced by the Al and/or H substitutions at relevant mantle *P-T* conditions can be of direct relevance to our understanding of the depth-dependent distributions of the regional seismic V_S anomalies in the lower mantle as discussed in the introduction. Therefore, we have compared our results with literature data to better evaluate the transition boundary as a function of Al and/or H contents. Based on

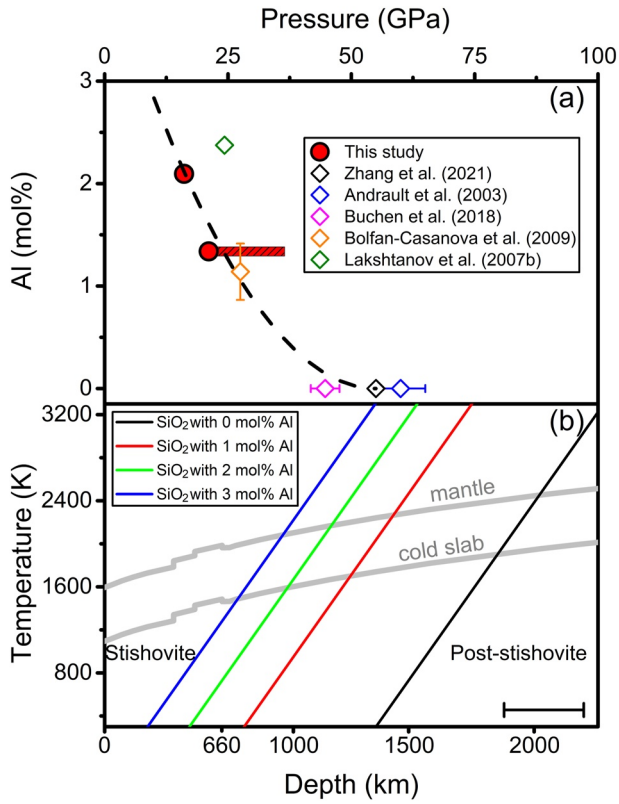

Figure 5. Post-stishovite phase transition boundary influenced by Al content in stishovite. (a) The post-stishovite transition pressure as a function of the Al content in mol% at 300 K. The dashed line is the best polynomial fit to our data using 55 GPa as the transition pressure of the pure SiO_2 by Zhang et al. (2021). The red shaded area in Al1.3-SiO_2 represents a pressure region where the stishovite and post-stishovite phases coexist (see Figures 2a and 2c). Literature results are also shown for comparison (Andrault et al., 2003; Bolfan-Casanova et al., 2009; Buchen et al., 2018; Lakshtanov et al., 2007b; Zhang et al., 2021). (b) Post-stishovite transition at high *P-T* conditions. A Clapeyron slope of 65 K/GPa is used for the post-stishovite transition (Fischer et al., 2018), where stishovite contains 0 (black), 1 (red), 2 (green), and 3 (blue) mol% Al, respectively. The horizontal bar at the bottom right indicates the coexistence range of the Al,H-bearing stishovite and post-stishovite phases, which is estimated from the coexistence of the A_g and A_g* modes in Al1.3-SiO_2 (Figures 2a and 2c). A typical normal mantle geotherm (Katsura et al., 2010) and a cold slab geotherm that is 500 K colder than a typical normal mantle geotherm (Tan et al., 2002) are shown as thick gray lines for comparison to the post-stishovite phase boundaries.

the Landau modeling at high pressure and 300 K, the P_C^* for Al1.3-SiO_2 and Al2.1-SiO_2 are ~21.1 and ~16.1 GPa, respectively, which are significantly lower than the P_C^* of 55 GPa in pure-endmember SiO_2 stishovite that contains ~19 wt. ppm water (Zhang et al., 2021).

Previous studies have showed that the post-stishovite transition pressure can be lowered by either the Al substitution (Bolfan-Casanova et al., 2009) or water incorporation (Nisr et al., 2017; Umemoto et al., 2016). Al and H incorporations in stishovite can occur via coupled $Al^{3+} + H^+$ for Si^{4+} in the octahedral site, together with Al^{3+} and O_V^{2+} substitution (Pawley et al., 1993). Hydrogen substitution in Al-free stishovite can also occur via $4H^+ \leftrightarrow Si^{4+}$ (Spektor et al., 2011). Importantly, previous studies have found that H solubility increases with the Al substitution in stishovite, but the Al:H ratio in stishovite is mostly near or below 3:1. Therefore, $2Al^{3+} + O_V^{2+} \leftrightarrow 2Si^{4+}$ substitution mechanism is expected to be more prevalent in hydrated Al-bearing stishovite in subducted basalts in the mantle (Pawley et al., 1993). Because our Al,H-bearing stishovite crystals only contain 0.25–0.27 wt% H_2O with 2.4–3.5 Al/H molar ratios, the P_C^* reduction can thus be mainly attributed to the $2Al^{3+} + O_V^{2+} \leftrightarrow 2Si^{4+}$ effect, together with some contributions from $4H^+ \leftrightarrow Si^{4+}$ substitution. Specifically, the $2Al^{3+} + O_V^{2+} \leftrightarrow 2Si^{4+}$ mechanism softens the stishovite's structure such that the post-stishovite shear distortion occurs more favorably under compression (Lakshtanov et al., 2007a).

Modeling the P_C^* as a function of Al contents using a polynomial function results in $Al = 0.0014\ P_C^{*2} - 0.154\ P_C^* + 4.235$ where Al is expressed in mol% and P_C^* is in GPa (Figure 5a). Using a Clapeyron slope of 65 K/GPa from a recent experimental study (Fischer et al., 2018), the post-stishovite transition can be extrapolated to high *P-T* conditions of the lower mantle: the transition pressure could be lowered by approximately 30 GPa in stishovite with 1 mol% Al and by 52 GPa with 3 mol% Al. Along a cold subducting slab which is taken as approximately 500 K colder than a typical normal mantle (Katsura et al., 2010; Tan et al., 2002), the post-stishovite transition is expected to occur at 740 km depth with 3 mol% Al and at 1,250 km depth with 1 mol% Al (Figure 5b). We should note that since the oceanic crust is thin and mainly exists on the surface of the subduction slabs, our cold-slab geotherm assumption, that is, 500 K colder than the surrounding mantle, should be taken as an upper bound of the temperature conditions.

4.3. Al and H Effects on the Sound Velocities Across the Post-Stishovite Transition

Our Landau modeling results provide full elastic moduli of the (Al,H)-bearing stishovite crystals across the post-stishovite transition at high pressure (Figure 6; refer to Tables S8 and S9 in Supporting Information S1 for numerical values of C_{ij}). Examinations of the pressure-dependent C_{ij} in the Al1.3-SiO_2 and Al2.1-SiO_2 crystals show that they are overall consistent with that of pure SiO_2 (Zhang et al., 2021), but the slopes across the transition are quite different. The (Al,H)-bearing stishovite crystals display softer C_{11} and stiffer C_{12} approaching the transition than the pure SiO_2 stishovite phase. These lead to the convergence of C_{11} and C_{12} at a lower P_C^* in the (Al,H)-bearing system. We should note that the $(C_{11}$-$C_{12})/2$ constant, which reflects the response of a crystal to deformation caused by shear stress along the [110] direction, is expected to vanish at the transition (Figure 6a). Similarly, the deviations between C_{12} and C_{22} and between C_{13} and C_{23} in the post-stishovite phase become larger (Figures 6a and 6b). In addition, our results show an enhanced reduction in the shear modulus and sound velocities (Figures 6c and 6d): the transition correlates with 49% μ reduction, 29% V_S reduction, and 12% V_P reduction as compared with reductions of 45% in μ, 26% in V_S, and 10% in V_P in pure SiO_2 post-stishovite transition (Zhang et al., 2021).

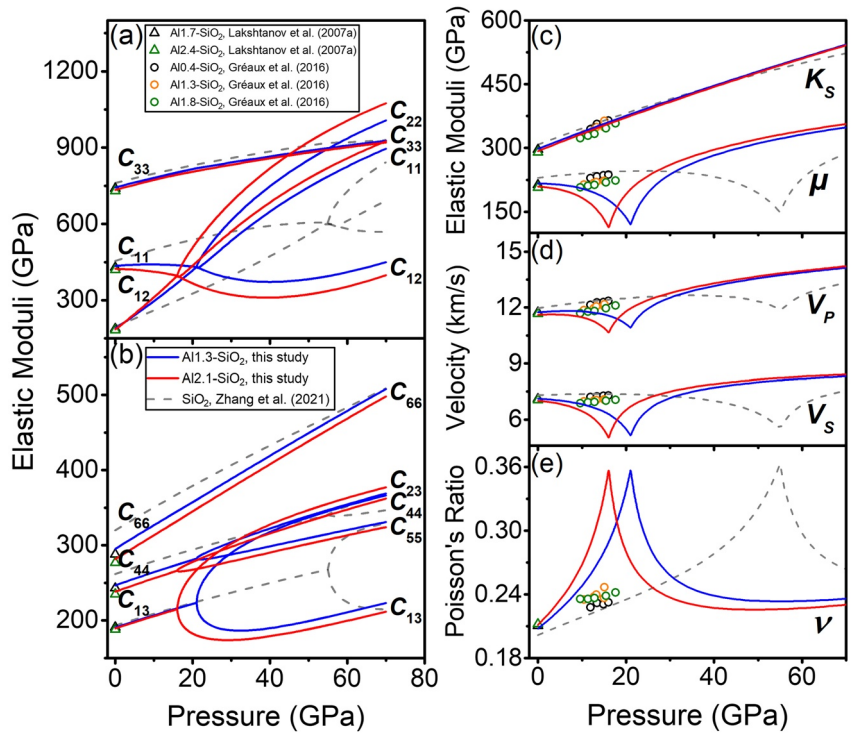

Figure 6. Modeled elasticity of the hydrated Al-bearing stishovite and post-stishovite at high pressure. (a) and (b) Elastic moduli C_{ij} of stishovite and post-stishovite at high pressure; (c) adiabatic bulk and shear moduli (K_S and μ) using the Voigt-Reuss-Hill averaging scheme (Hill, 1952); (d) aggregate compressional and shear wave velocities (V_P and V_S); (e) Poisson's ratio (ν). The Al1.3-SiO_2 (blue lines) and Al2.1-SiO_2 (red lines) stishovite crystals undergo the post-stishovite transition at 21.1 and 16.1 GPa, respectively, where their respective μ, V_P, and V_S drop drastically. ν jumps across the transition. Elasticity data for different compositions in the literature are also plotted for comparison (Gréaux et al., 2016; Lakshtanov et al., 2007a; Zhang et al., 2021).

4.4. Velocity Profiles of Subducted MORB Across the Post-Stishovite Transition in the Lower Mantle

The post-stishovite transition is known to occur in the subducted MORB such that sound velocity of the MORB materials can be useful in deciphering seismic results along subducting zone regions in the lower mantle. In our modeling to evaluate the effects of the post-stishovite transition on velocity profiles, we used elasticity of individual mineral phases in an aggregate with MORB composition along the aforementioned cold-slab geotherm. The mineralogy in the selected MORB composition contains 20 vol% stishovite, 30 vol% CF, 30 vol% Bgm, and 20 vol% CaPv in the lower mantle (Ishii et al., 2019). Thermoelastic parameters of these mineral phases, except CaPv, in our modeling are taken from this study, Zhang et al. (2021), and Xu et al. (2008). We should note that Xu et al. (2008) determined these parameters using previous elasticity data at high *P-T* (refer to Table S10 in Supporting Information S1 for details; Akaogi et al., 1999; Fei & Ahrens, 1995; Fiquet et al., 2000; Funamori et al., 1998; Kiefer et al., 2002; Liu et al., 1999; Murakami et al., 2003; Shim & Duffy, 2000; Sinogeikin et al., 2004; Smyth & McCormick, 1995; Wentzcovitch et al., 2004). On the other hand, thermoelastic parameters for CaPv are obtained by refitting combined elasticity data sets from Gréaux et al. (2019) and Sun et al. (2016) (Table S10 in Supporting Information S1). We should note that the CaPv data by Thomson et al. (2019) are not used here because they measured sound velocities at a nearly constant pressure such that some thermoelastic parameters cannot be reliably constrained such as pressure derivatives of K_S and μ. Mie-Grüneisen EOS and finite-strain theory are then used to calculate ρ, K_S, and μ of each mineral phase in the MORB mineralogy along a cold subducting slab based on the following equations (Stixrude & Lithgow-Bertelloni, 2005):

$$P = 3K_{T0}f(1+2f)^{5/2}\left[1+\frac{3}{2}\left(K'_{T0}-4\right)f\right]+\gamma\rho\Delta\mathfrak{V}_q \tag{17}$$

$$\begin{aligned}K_S =&(1+2f)^{5/2}\left[K_{S0}+\left(3K_{S0}K'_{S0}-5K_{S0}\right)f+\frac{27}{2}\left(K_{S0}K'_{S0}-4K_{S0}\right)f^2\right]\\&+(\gamma+1-q)\gamma\rho\triangle\mathfrak{V}_q-\gamma^2\rho\triangle\left(C_V T\right)\end{aligned} \tag{18}$$

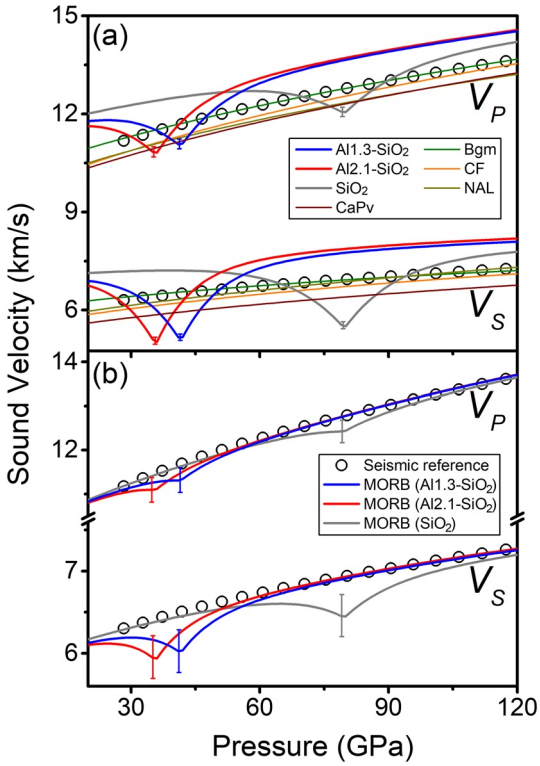

Figure 7. Modeled sound velocities of subducted MORB in the lower mantle. The modeled profiles are for a typical cold subducted slab mineralogy that is 500 K colder than a typical normal mantle (Ishii et al., 2019; Katsura et al., 2010; Tan et al., 2002). (a) V_P and V_S profiles of MORB materials. The SiO_2 with different Al contents and other MORB materials are shown as lines with different colors. (b) Aggregate velocities in the MORB mineralogy with 20 vol% stishovite with Al1.3-SiO_2 (blue lines), Al2.1-SiO_2 (red lines), or pure SiO_2 composition (gray lines). Propagated standard errors (±1σ uncertainties) in the model are shown as vertical bars with the same color as the corresponding lines in (a) and (b). Reference seismic profiles plotted as open circles represent seismic velocities in cold subduction regions that are about 1% higher than PREM at the same depth (Dziewonski & Anderson, 1981).

$$\mu = (1+2f)^{5/2}\left[\mu_0 + \left(3K_{S0}\mu_0' - 5\mu_0\right)f + \left(6K_{S0}\mu_0' - 24K_{S0} - 14\mu_0 + \frac{9}{2}K_{S0}K_{S0}'\right)f^2\right] - \eta_S\rho\Delta\mathfrak{O}_q \quad (19)$$

where f is the Eulerian finite strain, $f = \frac{1}{2}\left[\left(\frac{\rho}{\rho_0}\right)^{2/3} - 1\right]$; γ is the Grüneisen parameter, $\gamma = \frac{1}{6}(2f+1)(a_1 + a_2 f) / \left(1 + a_1 f + \frac{1}{2}a_2 f^2\right)$, where $a_1 = 6\gamma_0$, $a_2 = -12\gamma_0 + 36\gamma_0^2 - 18q\gamma_0$, and q is a constant; $\mathfrak{O}_q$ and C_V are internal energy and isochoric heat capacity, respectively, which can be calculated using the Debye model; K_{S0}' and μ_0' are the first-order pressure derivative of K_{S0} and μ_0, respectively; η_S is the first-order shear strain derivative of γ, $\eta_S = -\gamma + (2f+1)^2(\gamma_0 + \eta_{S0}) / \left(1 + a_1 f + \frac{1}{2}a_2 f^2\right)$; Δ means the difference between high temperature and 300 K; the subscript '0' denotes the ambient conditions.

We should note that the finite-strain model cannot be applied to evaluate the shear softening feature across the post-stishovite ferroelastic transition at high *P-T* conditions. Therefore, in addition to the finite-strain modeling, we have evaluated the shear modulus softening, $\Delta\mu$, across the transition at high *P-T* using the following equations (Helffrich et al., 2018):

$$\Delta\mu = A_0\left\{1 - \frac{2}{\pi}\left|arctan\left[\frac{P - P_{tr}(T)}{w}\right]\right|\right\}^2 \quad (20)$$

$$P_{tr}(T) = P_C^* + s(T - 300) \quad (21)$$

where A_0 is the maximum shear modulus softening in GPa, $P_{tr}(T)$ is the transition pressure in GPa at T in K with a Clapeyron slope s of 1/65 GPa/K, and w is the width of the phase transition in GPa. Fitting our modeled μ across the post-stishovite transition at 300 K with Equations 20 and 21 yields $A_0 = -148.4(7)$ GPa and $w = 14.7(1)$ GPa in Al1.3-SiO_2 and $A_0 = -152.4(9)$ GPa and $w = 13.9(2)$ GPa in Al2.1-SiO_2 (Figure 6c). After obtaining results from these aforementioned modeling efforts, ρ, K_S, and μ for the MORB mineralogy are calculated using the Voigt-Reuss-Hill scheme and volume ratios of the minerals to derive the V_S and V_P profiles of the aggregates in subducted MORB materials in the lower mantle (Figure 7) (Hill, 1952; Ishii et al., 2019).

5. Geophysical Implication

The anomalous elastic properties of stishovite across the second-order phase transformation have important implications for the interpretation of seismological observations. The large velocity contrast between the stishovite near the phase transformation and co-exiting minerals implies that there will be substantial seismic wave scattering at a boundary between stishovite-rich and stishovite-poor materials (Figure 7). First, for an obvious reason, the impact of stishovite on seismological observations depends on the amount of stishovite. For a typical lower mantle, stishovite exists only in regions occupied by subducted oceanic crust. Stishovite occupies approximately 20% in a typical oceanic crust subducted into the lower mantle (Ishii et al., 2019), whereas once subducted crust undergoes partial melting the amount of stishovite will increase substantially (Amulele et al., 2021). Second, since large velocity contrast (particularly in V_S) occurs at or near the depth of the second-order transformation, we expect to see the influence of stishovite in the depth corresponding to the depth of the phase transformation. Our and early experimental studies show that the depth at which the post-stishovite transition occurs strongly depends on the Al_2O_3 content ranging from ~800 to 1,600 km (Figure 5; Bolfan-Casanova et al., 2009; Lakshtanov et al., 2007b). The Al_2O_3 content in MORB materials ranges from ~4.3 to 8.1 mol% (Gale et al., 2013), which in turn affects

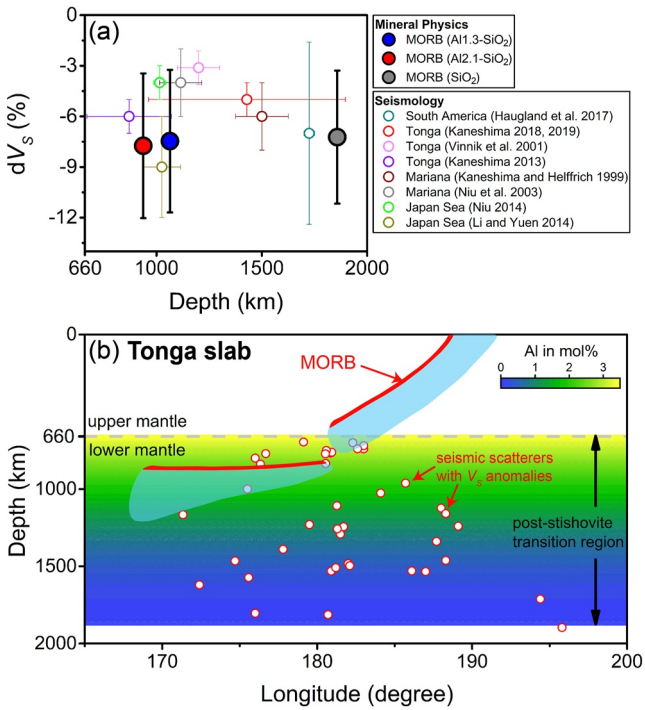

Figure 8. Seismic observations and mineral physics modeling of the depth-dependent V_S anomalies (dV_S) in the lower mantle. (a) dV_S observations of regional seismic V_S anomalies around subducting slabs at various depths are plotted as open circles. 20 vol% stishovite in a subducted MORB composition is used in our mineral physics model to account for the maximum V_S anomaly ($dV_{S,max}$) across the post-stishovite transition shown as solid circles. The $dV_{S,max}$ in % is calculated using the formula of $(V_{S,MORB}\text{-}V_{S,cold\ slab})/(V_{S,MORB} + V_{S,cold\ slab})\times 200$, where the $V_{S,cold\ slab}$ value is 1% higher than the V_S of PREM at the same depth (Dziewonski & Anderson, 1981) (Figure 7b). Literature data for seismic observations include Haugland et al. (2017), Kaneshima (2018, 2019), Vinnik et al. (2001), Kaneshima (2013), Kaneshima and Helffrich (1999), Niu et al. (2003), Niu (2014), and Li and Yuen (2014). Note that some of these studies have only reported lower bound of the V_S anomaly (Kaneshima, 2013, 2018; Kaneshima & Helffrich, 1999). (b) Depth-longitude schematics for the seismic dV_S anomalies and the post-stishovite transition along the Tonga subduction region. The color shaded area represents the post-stishovite transition region scaled with the Al content in a color scale shown on the top right. Reported seismic V_S anomalies (red open circles) with different latitudes in the Tonga region are projected onto the two-dimensional schematic (Kaneshima, 2009, 2013, 2018, 2019; Kaneshima & Helffrich, 2010). The geometry and position of the Tonga subducting slab are drawn according to previous seismic images (Fukao & Obayashi, 2013).

the amount of Al in natural stishovite. Considering MORB materials with a typical ~6.8 mol% Al, stishovite is expected to contain ~1.3 mol% Al from 800 to 1,600 km depth (Figure S2 in Supporting Information S1).

Indeed, seismic wave scattering is often reported in regions linked to subduction zones from top- to mid-lower mantle. These subduction regions include South America (Haugland et al., 2017), Tonga (Kaneshima, 2013, 2018, 2019; Vinnik et al., 2001), Mariana (Kaneshima & Helffrich, 1999; Niu et al., 2003), and Japan sea (Li & Yuen, 2014; Niu, 2014). The magnitudes of the seismically-observed V_S anomalies are generally consistent with our modeled maximum V_S anomaly ($dV_{S,max}$) of 7–8(±4)% in MORB with 20% silica undergoing the post-stishovite transition (Figure 8a). Seismic observations also show that the number of these anomalies decreases with depth and the majority of these seismic scatterers (~85%) occurs above 1,600 km depth (Kaneshima, 2013, 2018, 2019). These observations can be interpreted as a result of the Al-dependent post-stishovite transition in subducted MORB materials as well as the broad V_S reduction across the ferroelastic transition (Figure 8b).

Our results can also have implications to our understanding of the water circulation and storage in the deep mantle. MORB materials contain some water due to the hydrothermal processes. The subduction of MORB materials can bring a certain amount of water into the mantle through hydrogen dissolved in NAMs. Stishovite is one of the NAMs and can accommodate a certain amount of water in its lattice along the subduction processes (Lin et al., 2019; Litasov et al., 2007; Ohtani, 2020). As the slabs reach the 660-km boundary layer in some subduction regions, dehydration-induced partial melting can occur in the shallow lower mantle (Liu et al., 2016; Schmandt et al., 2014) and produce Al-bearing stishovite with approximately 700 wt. ppm H_2O (Amulele et al., 2021). Our Al,H-bearing stishovite can contain 0.25 and 0.27 wt% H_2O with an Al:H ratio close to 2:1 (Figure 1d). Using 2:1 for the Al:H ratio in natural stishovite in a typical MORB composition, stishovite with 1.3 mol% Al_2O_3 would contain approximately 0.65 mol% H (or 0.3 wt% H_2O) in the upper part of the lower mantle. The 0.3 wt% H_2O in stishovite is significantly larger than the water solubility of ~0.1 wt% in other MORB components such as Bgm and NAL phase (Fu et al., 2019; Wu et al., 2016), making the Al,H-bearing stishovite a plausible water carrier along the subduction slabs into the lower mantle.

Previous studies have showed that hydration in stishovite can significantly enhance its electrical conductivity by two orders of magnitude at 12 GPa and high temperature (Yoshino et al., 2014). Electromagnetic observations of high electrical conductivity regions along circum-Pacific subducting slabs in the shallow lower mantle (Kelbert et al., 2009) may be interpreted as a result of the presence of hydrated silica-rich materials.

6. Conclusion

We have studied the vibrational Raman modes and lattice parameters of two Al,H-bearing stishovite crystals, Al1.3-SiO_2 with 0.55 mol% H and Al2.1-SiO_2 with 0.59 mol% H, across the post-stishovite transition at high pressure. The experimental results are used to evaluate the Al and Al/H substitutional effects on the post-stishovite phase boundary and the elasticity across the post-stishovite transition. Landau theory modeling of the experimental data is used to derive the transition pressure and full elasticity across the transition, where the soft B_{1g} mode becomes the hard A_g mode, the a axis splits into the a and b axis, the $(C_{11}\text{-}C_{12})/2$ approaches zero, and the V_S displays −29% softening. The Al and H incorporation reduces the transition pressure to 21.1 GPa in Al1.3-

SiO_2 and 16.1 GPa in Al2.1-SiO_2. We have modeled high *P-T* phase boundary and elasticity of stishovite and post-stishovite for a MORB mineralogy with 20 vol% stishovite. For a typical MORB composition where stishovite is expected to contain 1.3 mol% Al, the post-stishovite transition can cause for −7(4)% $dV_{S,max}$ in subducted MORB at 1064 km depth. These results help explain depth-dependent V_S anomaly distributions of some regional small-scale scatterers especially for the *S*-to-*P* scattering along the Tonga subduction region. The Al,H-bearing stishovite can also accommodate approximately 0.3 wt% H_2O via the coupled substitution mechanism of $Al^{3+} + H^+ \leftrightarrow Si^{4+}$ in the upper part of the lower mantle. The lattice-bonded water is expected to remain stable in the post-stishovite phase. The water in stishovite and post-stishovite phases could affect electrical conductivity of silica-rich materials in the region.

Conflict of Interest

The authors declare no conflicts of interest relevant to this study.

Data Availability Statement

EPMA results are listed in Table S1 in Supporting Information S1. Raman data for Figure 2 are available in Tables S2–S4 in Supporting Information S1. XRD data for Figure 3 are available in Tables S5–S7 in Supporting Information S1. Numerical values of the modeled C_{ij} for Figure 6 are listed in Tables S8 and S9 in Supporting Information S1. Thermoelastic parameters used in the modeling are listed in Table S10 in Supporting Information S1. All these data can also be downloaded online (https://zenodo.org/record/6391581)

Acknowledgments
We thank N. Purevjav for her assistance on the synthesis and characterization of the single-crystal stishovite. We also thank Jennifer Kung, Vincent Jian and Ching-Chien Li for their assistances in FTIR measurements. Diffraction experiments were performed at 13ID-D, GSECARS. GSECARS was supported by the National Science Foundation (EAR-0622171). This research used resources of the Advanced Photon Source, a U.S. Department of Energy (DOE) Office of Science User Facility operated for the DOE Office of Science by Argonne National Laboratory under Contract No. DE-AC02-06CH11357. J.F. Lin acknowledges support from Geophysics Program of the U.S. National Science Foundation (EAR-1916941 and EAR-2001381) and the Joint-Use User Program of the Institute for Planetary Materials, Okayama University. T. Okuchi acknowledges support from JSPS KAKENHI (17H01172).

References

Akaogi, M., Hamada, Y., Suzuki, T., Kobayashi, M., & Okada, M. (1999). High pressure transitions in the system MgAl2O4–CaAl2O4: A new hexagonal aluminous phase with implication for the lower mantle. *Physics of the Earth and Planetary Interiors*, *115*, 67–77. https://doi.org/10.1016/s0031-9201(99)00076-x

Amulele, G., Karato, S. i., & Girard, J. (2021). Melting of bridgmanite under hydrous shallow lower mantle conditions. *Journal of Geophysical Research: Solid Earth*, *126*, e2021JB022222. https://doi.org/10.1029/2021jb022222

Andrault, D., Angel, R. J., Mosenfelder, J. L., & Bihan, T. L. (2003). Equation of state of stishovite to lower mantle pressures. *American Mineralogist*, *88*, 301–307. https://doi.org/10.2138/am-2003-2-307

Asahara, Y., Hirose, K., Ohishi, Y., Hirao, N., Ozawa, H., & Murakami, M. (2013). Acoustic velocity measurements for stishovite across the post-stishovite phase transition under deviatoric stress: Implications for the seismic features of subducting slabs in the mid-mantle. *American Mineralogist*, *98*, 2053–2062. https://doi.org/10.2138/am.2013.4145

Birch, F. (1947). Finite elastic strain of cubic crystals. *Physical Review*, *71*, 809–824. https://doi.org/10.1103/physrev.71.809

Bolfan-Casanova, N., Andrault, D., Amiguet, E., & Guignot, N. (2009). Equation of state and post-stishovite transformation of Al-bearing silica up to 100 GPa and 3000 K. *Physics of the Earth and Planetary Interiors*, *174*, 70–77. https://doi.org/10.1016/j.pepi.2008.06.024

Buchen, J., Marquardt, H., Schulze, K., Speziale, S., Boffa Ballaran, T., Nishiyama, N., & Hanfland, M. (2018). Equation of state of polycrystalline stishovite across the tetragonal-orthorhombic phase transition. *Journal of Geophysical Research: Solid Earth*, *123*, 7347–7360. https://doi.org/10.1029/2018jb015835

Carpenter, M. A., Hemley, R. J., & Mao, H. k. (2000). High-pressure elasticity of stishovite and the P42/mnm⇌ Pnnm phase transition. *Journal of Geophysical Research*, *105*, 10807–10816. https://doi.org/10.1029/1999jb900419

Dziewonski, A. M., & Anderson, D. L. (1981). Preliminary reference Earth model. *Physics of the Earth and Planetary Interiors*, *25*, 297–356. https://doi.org/10.1016/0031-9201(81)90046-7

Fei, Y., & Ahrens, T. (1995). Thermal expansion. *Mineral physics and crystallography: A handbook of physical constants*, *2*, 29–44.

Fei, Y., Ricolleau, A., Frank, M., Mibe, K., Shen, G., & Prakapenka, V. (2007). Toward an internally consistent pressure scale. *Proceedings of the National Academy of Sciences*, *104*, 9182–9186. https://doi.org/10.1073/pnas.0609013104

Fiquet, G., Dewaele, A., Andrault, D., Kunz, M., & Le Bihan, T. (2000). Thermoelastic properties and crystal structure of MgSiO3 perovskite at lower mantle pressure and temperature conditions. *Geophysical Research Letters*, *27*, 21–24. https://doi.org/10.1029/1999gl008397

Fischer, R. A., Campbell, A. J., Chidester, B. A., Reaman, D. M., Thompson, E. C., Pigott, J. S., et al. (2018). Equations of state and phase boundary for stishovite and CaCl2-type SiO2. *American Mineralogist*, *103*, 792–802. https://doi.org/10.2138/am-2018-6267

Fu, S., Yang, J., Karato, S. i., Vasiliev, A., Presniakov, M. Y., Gavrilliuk, A. G., et al. (2019). Water concentration in single-crystal (Al, Fe)-bearing bridgmanite grown from the hydrous melt: Implications for dehydration melting at the topmost lower mantle. *Geophysical Research Letters*. https://doi.org/10.1029/2019gl084630

Fukao, Y., & Obayashi, M. (2013). Subducted slabs stagnant above, penetrating through, and trapped below the 660 km discontinuity. *Journal of Geophysical Research: Solid Earth*, *118*, 5920–5938. https://doi.org/10.1002/2013jb010466

Funamori, N., Jeanloz, R., Nguyen, J. H., Kavner, A., Caldwell, W. A., Fujino, K., et al. (1998). High-pressure transformations in MgAl2O4. *Journal of Geophysical Research*, *103*(B9), 20813–20818.

Gale, A., Dalton, C. A., Langmuir, C. H., Su, Y., & Schilling, J. G. (2013). The mean composition of ocean ridge basalts. *Geochemistry, Geophysics, Geosystems*, *14*, 489–518. https://doi.org/10.1029/2012gc004334

Gréaux, S., Irifune, T., Higo, Y., Tange, Y., Arimoto, T., Liu, Z., & Yamada, A. (2019). Sound velocity of CaSiO 3 perovskite suggests the presence of basaltic crust in the Earth's lower mantle. *Nature*, *565*(7738), 218.

Gréaux, S., Kono, Y., Wang, Y., Yamada, A., Zhou, C., Jing, Z., et al. (2016). Sound velocities of aluminum-bearing stishovite in the mantle transition zone. *Geophysical Research Letters*, *43*, 4239–4246.

Haugland, S. M., Ritsema, J., Kaneshima, S., & Thorne, M. S. (2017). Estimate of the rigidity of eclogite in the lower mantle from waveform modeling of broadband S-to-P wave conversions. *Geophysical Research Letters*, *44*(11), 11778–11784. https://doi.org/10.1002/2017gl075463

Helffrich, G., Ballmer, M. D., & Hirose, K. (2018). Core-exsolved SiO2 dispersal in the Earth's mantle. *Journal of Geophysical Research: Solid Earth*, *123*, 176–188. https://doi.org/10.1002/2017jb014865

Hemley, R., Shu, J., Carpenter, M., Hu, J., Mao, H., & Kingma, K. (2000). Strain/order parameter coupling in the ferroelastic transition in dense SiO2. *Solid State Communications*, *114*, 527–532. https://doi.org/10.1016/s0038-1098(00)00099-5

Hill, R. (1952). The elastic behaviour of a crystalline aggregate. *Proceedings of the Physical Society Section A*, *65*, 349–354. https://doi.org/10.1088/0370-1298/65/5/307

Hirose, K., Takafuji, N., Sata, N., & Ohishi, Y. (2005). Phase transition and density of subducted MORB crust in the lower mantle. *Earth and Planetary Science Letters*, *237*, 239–251. https://doi.org/10.1016/j.epsl.2005.06.035

Irifune, T., Shinmei, T., McCammon, C. A., Miyajima, N., Rubie, D. C., & Frost, D. J. (2010). Iron partitioning and density changes of pyrolite in Earth's lower mantle. *Science*, *327*, 193–195. https://doi.org/10.1126/science.1181443

Ishii, T., Kojitani, H., & Akaogi, M. (2019). Phase relations of harzburgite and MORB up to the uppermost lower mantle conditions: Precise comparison with pyrolite by multisample cell high-pressure experiments with implication to dynamics of subducted slabs. *Journal of Geophysical Research: Solid Earth*. https://doi.org/10.1029/2018jb016749

Kaneshima, S. (2009). Seismic scatterers at the shallowest lower mantle beneath subducted slabs. *Earth and Planetary Science Letters*, *286*, 304–315. https://doi.org/10.1016/j.epsl.2009.06.044

Kaneshima, S. (2013). Lower mantle seismic scatterers below the subducting Tonga slab: Evidence for slab entrainment of transition zone materials. *Physics of the Earth and Planetary Interiors*, *222*, 35–46. https://doi.org/10.1016/j.pepi.2013.07.001

Kaneshima, S. (2018). Seismic scatterers in the mid-lower mantle beneath Tonga-Fiji. *Physics of the Earth and Planetary Interiors*, *274*, 1–13. https://doi.org/10.1016/j.pepi.2017.09.007

Kaneshima, S. (2019). Seismic scatterers in the lower mantle near subduction zones. *Geophysical Journal International*, *218*, 1873–1891. https://doi.org/10.1093/gji/ggz241

Kaneshima, S., & Helffrich, G. (1999). Dipping low-velocity layer in the mid-lower mantle: Evidence for geochemical heterogeneity. *Science*, *283*, 1888–1892. https://doi.org/10.1126/science.283.5409.1888

Kaneshima, S., & Helffrich, G. (2010). Small scale heterogeneity in the mid-lower mantle beneath the circum-Pacific area. *Physics of the Earth and Planetary Interiors*, *183*, 91–103. https://doi.org/10.1016/j.pepi.2010.03.011

Karki, B. B., Stixrude, L., & Crain, J. (1997). Ab initio elasticity of three high-pressure polymorphs of silica. *Geophysical Research Letters*, *24*, 3269–3272. https://doi.org/10.1029/97gl53196

Katsura, T., Yoneda, A., Yamazaki, D., Yoshino, T., & Ito, E. (2010). Adiabatic temperature profile in the mantle. *Physics of the Earth and Planetary Interiors*, *183*, 212–218. https://doi.org/10.1016/j.pepi.2010.07.001

Kelbert, A., Schultz, A., & Egbert, G. (2009). Global electromagnetic induction constraints on transition-zone water content variations. *Nature*, *460*, 1003–1006. https://doi.org/10.1038/nature08257

Kiefer, B., Stixrude, L., & Wentzcovitch, R. (2002). Elasticity of (Mg, Fe) SiO3-perovskite at high pressures. *Geophysical Research Letters*, *29*, 34–313434. https://doi.org/10.1029/2002gl014683

Kingma, K. J., Cohen, R. E., Hemley, R. J., & Mao, H.-k. (1995). Transformation of stishovite to a denser phase at lower-mantle pressures. *Nature*, *374*, 243–245. https://doi.org/10.1038/374243a0

Lakshtanov, D. L., Litasov, K. D., Sinogeikin, S. V., Hellwig, H., Li, J., Ohtani, E., & Bass, J. D. (2007a). Effect of Al3+ and H+ on the elastic properties of stishovite. *American Mineralogist*, *92*, 1026–1030. https://doi.org/10.2138/am.2007.2294

Lakshtanov, D. L., Sinogeikin, S. V., Litasov, K. D., Prakapenka, V. B., Hellwig, H., Wang, J., et al. (2007b). The post-stishovite phase transition in hydrous alumina-bearing SiO2 in the lower mantle of the Earth. *Proceedings of the National Academy of Sciences*, *104*, 13588–13590. https://doi.org/10.1073/pnas.0706113104

Li, B., Rigden, S. M., & Liebermann, R. C. (1996). Elasticity of stishovite at high pressure. *Physics of the Earth and Planetary Interiors*, *96*, 113–127. https://doi.org/10.1016/0031-9201(96)03144-5

Li, J., & Yuen, D. A. (2014). Mid-mantle heterogeneities associated with Izanagi plate: Implications for regional mantle viscosity. *Earth and Planetary Science Letters*, *385*, 137–144. https://doi.org/10.1016/j.epsl.2013.10.042

Lin, Y., Hu, Q., Meng, Y., Walter, M., & Mao, H.-K. (2019). Evidence for the stability of ultrahydrous stishovite in Earth's lower mantle. *Proceedings of the National Academy of Sciences*.

Litasov, K. D., Kagi, H., Shatskiy, A., Ohtani, E., Lakshtanov, D. L., Bass, J. D., & Ito, E. (2007). High hydrogen solubility in Al-rich stishovite and water transport in the lower mantle. *Earth and Planetary Science Letters*, *262*, 620–634. https://doi.org/10.1016/j.epsl.2007.08.015

Liu, J., Zhang, J., Flesch, L., Li, B., Weidner, D. J., & Liebermann, R. C. (1999). Thermal equation of state of stishovite. *Physics of the Earth and Planetary Interiors*, *112*, 257–266. https://doi.org/10.1016/s0031-9201(99)00037-0

Liu, Z., Park, J., & Karato, S. i. (2016). Seismological detection of low-velocity anomalies surrounding the mantle transition zone in Japan subduction zone. *Geophysical Research Letters*, *43*, 2480–2487. https://doi.org/10.1002/2015gl067097

Murakami, M., Hirose, K., Ono, S., & Ohishi, Y. (2003). Stability of $CaCl_2$-type and α-PbO_2-type SiO_2 at high pressure and temperature determined by in-situ X-ray measurements. *Geophysical Research Letters*, *30*. https://doi.org/10.1029/2002gl016722

Nisr, C., Leinenweber, K., Prakapenka, V., Prescher, C., Tkachev, S., & Dan Shim, S. H. (2017). Phase transition and equation of state of dense hydrous silica up to 63 GPa. *Journal of Geophysical Research: Solid Earth*. https://doi.org/10.1002/2017jb014055

Nisr, C., Leinenweber, K., Prakapenka, V., Prescher, C., Tkachev, S., & Dan Shim, S. H. (2017). Phase transition and equation of state of dense hydrous silica up to 63 GPa. *Journal of Geophysical Research: Solid Earth*.

Nisr, C., Shim, S.-H., Leinenweber, K., & Chizmeshya, A. (2017). Raman spectroscopy of water-rich stishovite and dense high-pressure silica up to 55 GPa. *American Mineralogist*, *102*(11), 2180–2189.

Niu, F. (2014). Distinct compositional thin layers at mid-mantle depths beneath northeast China revealed by the USArray. *Earth and Planetary Science Letters*, *402*, 305–312. https://doi.org/10.1016/j.epsl.2013.02.015

Niu, F., Kawakatsu, H., & Fukao, Y. (2003). Seismic evidence for a chemical heterogeneity in the midmantle: A strong and slightly dipping seismic reflector beneath the Mariana subduction zone. *Journal of Geophysical Research*, *108*. https://doi.org/10.1029/2002jb002384

Ohtani, E. (2020). The role of water in Earth's mantle. *National Science Review*, *7*, 224–232. https://doi.org/10.1093/nsr/nwz071

Okuchi, T., Purevjav, N., Tomioka, N., Lin, J.-F., Kuribayashi, T., Schoneveld, L., et al. (2015). Synthesis of large and homogeneous single crystals of water-bearing minerals by slow cooling at deep-mantle pressures. *American Mineralogist*, *100*, 1483–1492. https://doi.org/10.2138/am-2015-5237

Ono, S., Ito, E., & Katsura, T. (2001). Mineralogy of subducted basaltic crust (MORB) from 25 to 37 GPa, and chemical heterogeneity of the lower mantle. *Earth and Planetary Science Letters*, *190*, 57–63. https://doi.org/10.1016/s0012-821x(01)00375-2

Paterson, M. (1982). The determination of hydroxyl by infrared absorption in quartz, silicate glasses and similar materials. *Bulletin de Mineralogie*, *105*, 20–29. https://doi.org/10.3406/bulmi.1982.7582

Pawley, A. R., McMillan, P. F., & Holloway, J. R. (1993). Hydrogen in stishovite, with implications for mantle water content. *Science*, *261*, 1024–1026. https://doi.org/10.1126/science.261.5124.1024

Prescher, C., & Prakapenka, V. B. (2015). Dioptas: A program for reduction of two-dimensional X-ray diffraction data and data exploration. *High Pressure Research*, *35*, 223–230. https://doi.org/10.1080/08957959.2015.1059835

Ringwood, A. E. (1975). *Composition and petrology of the Earth's mantle* (Vol. 618). MacGraw-Hill.

Rost, S., Garnero, E. J., & Williams, Q. (2008). Seismic array detection of subducted oceanic crust in the lower mantle. *Journal of Geophysical Research*, *113*. https://doi.org/10.1029/2007jb005263

Salje, E. (1990). Phase transitions in ferroelastic and co-elastic crystals. *Ferroelectrics*, *104*, 111–120. https://doi.org/10.1080/00150199008223816

Schmandt, B., Jacobsen, S. D., Becker, T. W., Liu, Z., & Dueker, K. G. (2014). Dehydration melting at the top of the lower mantle. *Science*, *344*, 1265–1268. https://doi.org/10.1126/science.1253358

Shieh, S. R., Duffy, T. S., & Li, B. (2002). Strength and elasticity of S i O 2 across the stishovite–C a C l 2-type structural phase boundary. *Physical Review Letters*, *89*, 255507. https://doi.org/10.1103/physrevlett.89.255507

Shim, S.-H., & Duffy, T. S. (2000). Constraints on the PVT equation of state of MgSiO3 perovskite. *American Mineralogist*, *85*, 354–363. https://doi.org/10.2138/am-2000-2-314

Sinogeikin, S. V., Zhang, J., & Bass, J. D. (2004). Elasticity of single crystal and polycrystalline MgSiO3 perovskite by Brillouin spectroscopy. *Geophysical Research Letters*, *31*. https://doi.org/10.1029/2004gl019559

Smyth, J. R., & McCormick, T. C. (1995). Crystallographic data for minerals. *Mineral physics and crystallography: A handbook of physical constants*, *2*, 1–17.

Spektor, K., Nylen, J., Stoyanov, E., Navrotsky, A., Hervig, R. L., Leinenweber, K., et al. (2011). Ultrahydrous stishovite from high-pressure hydrothermal treatment of SiO2. *Proceedings of the National Academy of Sciences*, *108*, 20918–20922. https://doi.org/10.1073/pnas.1117152108

Stixrude, L., & Lithgow-Bertelloni, C. (2005). Thermodynamics of mantle minerals—I. Physical properties. *Geophysical Journal International*, *162*, 610–632. https://doi.org/10.1111/j.1365-246x.2005.02642.x

Sun, N., Mao, Z., Yan, S., Wu, X., Prakapenka, V. B., & Lin, J. F. (2016). Confirming a pyrolitic lower mantle using self-consistent pressure scales and new constraints on CaSiO3 perovskite. *Journal of Geophysical Research: Solid Earth*, *121*, 4876–4894. https://doi.org/10.1002/2016jb013062

Tan, E., Gurnis, M., & Han, L. (2002). Slabs in the lower mantle and their modulation of plume formation. *Geochemistry, Geophysics, Geosystems*, *3*, 1–24. https://doi.org/10.1029/2001gc000238

Thomson, A., Crichton, W., Brodholt, J., Wood, I., Siersch, N., Muir, J., et al. (2019). Seismic velocities of CaSiO 3 perovskite can explain LLSVPs in Earth's lower mantle. *Nature*, *572*, 643–647. https://doi.org/10.1038/s41586-019-1483-x

Umemoto, K., Kawamura, K., Hirose, K., & Wentzcovitch, R. M. (2016). Post-stishovite transition in hydrous aluminous SiO 2. *Physics of the Earth and Planetary Interiors*, *255*, 18–26. https://doi.org/10.1016/j.pepi.2016.03.008

Vinnik, L., Kato, M., & Kawakatsu, H. (2001). Search for seismic discontinuities in the lower mantle. *Geophysical Journal International*, *147*, 41–56. https://doi.org/10.1046/j.1365-246x.2001.00516.x

Wang, W., Xu, Y., Sun, D., Ni, S., Wentzcovitch, R., & Wu, Z. (2020). Velocity and density characteristics of subducted oceanic crust and the origin of lower-mantle heterogeneities. *Nature Communications*, *11*, 1–8. https://doi.org/10.1038/s41467-019-13720-2

Wentzcovitch, R., Karki, B., Cococcioni, M., & De Gironcoli, S. (2004). Thermoelastic properties of M g S i O 3-perovskite: Insights on the nature of the Earth's lower mantle. *Physical Review Letters*, *92*, 018501. https://doi.org/10.1103/physrevlett.92.018501

Wu, Y., Yang, J., Wu, X., Song, M., Yoshino, T., Zhai, S., et al. (2016). Elasticity of single-crystal NAL phase at high pressure: A potential source of the seismic anisotropy in the lower mantle. *Journal of Geophysical Research: Solid Earth*, *121*, 5696–5707. https://doi.org/10.1002/2016jb013136

Xu, F., Yamazaki, D., Sakamoto, N., Sun, W., Fei, H., & Yurimoto, H. (2017). Silicon and oxygen self-diffusion in stishovite: Implications for stability of SiO2-rich seismic reflectors in the mid-mantle. *Earth and Planetary Science Letters*, *459*, 332–339. https://doi.org/10.1016/j.epsl.2016.11.044

Xu, W., Lithgow-Bertelloni, C., Stixrude, L., & Ritsema, J. (2008). The effect of bulk composition and temperature on mantle seismic structure. *Earth and Planetary Science Letters*, *275*, 70–79. https://doi.org/10.1016/j.epsl.2008.08.012

Yang, J., Tong, X., Lin, J.-F., Okuchi, T., & Tomioka, N. (2015). Elasticity of ferropericlase across the spin crossover in the Earth's lower mantle. *Scientific Reports*, *5*. https://doi.org/10.1038/srep17188

Yang, R., & Wu, Z. (2014). Elastic properties of stishovite and the CaCl 2-type silica at the mantle temperature and pressure: An ab initio investigation. *Earth and Planetary Science Letters*, *404*, 14–21. https://doi.org/10.1016/j.epsl.2014.07.020

Yoshino, T., Shimojuku, A., & Li, D. (2014). Electrical conductivity of stishovite as a function of water content. *Physics of the Earth and Planetary Interiors*, *227*, 48–54. https://doi.org/10.1016/j.pepi.2013.12.003

Zedgenizov, D., Shatsky, V., Panin, A., Evtushenko, O., Ragozin, A., & Kagi, H. (2015). Evidence for phase transitions in mineral inclusions in superdeep diamonds of the São Luiz deposit (Brazil). *Russian Geology and Geophysics*, *56*, 296–305. https://doi.org/10.1016/j.rgg.2015.01.021

Zhang, Y., Fu, S., Wang, B., & Lin, J.-F. (2021). Elasticity of a pseudoproper ferroelastic transition from stishovite to post-stishovite at high pressure. *Physical Review Letters*, *126*, 025701. https://doi.org/10.1103/physrevlett.126.025701

References From the Supporting Information

Lakshtanov, D. L., Vanpeteghem, C. B., Jackson, J. M., Bass, J. D., Shen, G., Prakapenka, V. B., et al. (2005). The equation of state of Al, H-bearing SiO2 stishovite to 58 GPa. *Physics and Chemistry of Minerals*, *32*(7), 466–470.

Litasov, K. D., & Ohtani, E. (2005). Phase relations in hydrous MORB at 18–28 GPa: Implications for heterogeneity of the lower mantle. *Physics of the Earth and Planetary Interiors*, *150*(4), 239–263.

Ono, S., Suto, T., Hirose, K., Kuwayama, Y., Komabayashi, T., & Kikegawa, T. (2002). Equation of state of Al-bearing stishovite to 40 GPa at 300 K. *American Mineralogist*, *87*(10), 1486–1489.

Tellinghuisen, J. (2001). Statistical error propagation. *The Journal of Physical Chemistry A*, *105*(15), 3917–3921.

Tsuchiya, T. (2011). Elasticity of subducted basaltic crust at the lower mantle pressures: Insights on the nature of deep mantle heterogeneity. *Physics of the Earth and Planetary Interiors*, *188*(3–4), 142–149.